Aeroacoustics Conferences
June 14-17, 2022, Southampton, UK
28th AIAA/CEAS Aeroacoustics 2022 Conference

10.2514/6.2022-3032

Turbulence Ingestion of a Non-Axisymmetric Wake by an Open Rotor

Jarrod T. Banks *, Humza Butt †, William N. Alexander ‡, and William J. Devenport §,
Center for Research in Experimental Aero/Hydrodynamic Technology, Blacksburg, VA,24060

N. Agastya Balantrapu ¶
Princeton University, Princeton, NJ, 08544

Christopher J. Hickling ‖
Naval Surface Warfare Center, Carderock, MD, 20817

Stewart Glegg**
Florida Atlantic University, Boca Raton, FL, 33431

The turbulent inflow for a rotor at the tail of a body of revolution was measured for three configurations. The body of revolution consists of a 2:1 ellipsoidal nose, a straight midbody and a 20°tail ramp that narrows the body towards the rotor inlet. The rotor is placed at the back of the body of revolution to ingest the turbulent boundary layer grown over the length of the body of revolution. Measurements of the mean body pressure, velocity field, and radiated acoustic sound were taken principally at $R_e = 600,000$ for a range of advance ratios ($J = 1.10, 1.27, 1.34, 1.44$). Comparisons were made for the two-point correlation function evolution and turbulence characteristics of the 0°angle of attack, 5°pitch down angle of attack, and 5°yaw starboard angle of attack using time resolved particle image velocimetry. Phase correlated structures at various thrusting conditions are noted in the turbulence profiles for the 5°pitch down case. The deformation of the two-point correlation function along a streamline was found to be greater for the 5°pitch down configuration than the 5°yaw starboard configuration. The broadband sound generated by the rotor was found to be principally dominated by the turbulence in the region at 90°to the windward side of the tail ramp due to the higher turbulence levels here.

Nomenclature

c_∞	=	sound speed
D	=	body of revolution diameter (mm)
dB	=	decibals relative to $20\mu Pa$
f	=	frequency (Hz)
J	=	advance ratio
L_{st}	=	Taylor lengthscale (mm)
L_s	=	Lengthscale (mm)
RPM	=	revolutions per minute
$\overline{U}$	=	mean velocity (m/s)
u	=	fluctuating velocity (m/s)
x, y, z	=	body fixed coordinate system
X, Y, Z	=	test section fixed coordinate system
δ	=	boundary layer thickness (mm)

*Graduate Research Associate, Center for Research in Experimental Aero/Hydrodynamic Technology, AIAA Student Member
†Graduate Research Associate, Center for Research in Experimental Aero/hydrodynamic technology, AIAA Student Member
‡Assistant Professor, Center for Research in Experimental Aero/Hydrodynamic Technology, Associate Fellow AIAA.
§Crofton Professor of Engineering, Center for Research in Experimental Aero/Hydrodynamic Technology, Fellow AIAA.
¶Assistant Professor, Princeton University, AIAA Member
‖Research Scientist, Naval Surface Warfare Center, AIAA Member.
**Professor, Department of Ocean and Mechanical Engineering, Associate Fellow AIAA.

Γ	=	timescales (s)
τ	=	time delay (s)
ρ	=	correlation function
Ω	=	rotational speed (rpm)
Subscripts		
c	=	convection
e	=	edge
sp	=	spanwise
s	=	streamwise
x, y, z	=	body fixed coordinate system
∞	=	infinity

I. Introduction

Rotors and lifting surfaces generate leading edge noise when they interact with turbulent shear flows, for example boundary layers developed over the surface of a vehicle such as in many pusher and VTOL rotorcraft, submarines, and small UAV's. Typically these shear layers are also under the influence of some form of pressure gradient induced by the vehicle body surface. The ingested turbluence is radiated as broadband noise with spectral humps centered at frequencies slightly above the harmonics of the rotor blade passage frequency. Estimations of the intensity of the broadband noise have been attempted by Devenport and Glegg [1] by estimating the turbulence as a sum of several proper orthogonal decomposition modes. The input to this method is the full two point correlation tensor. Estimating the two point correlation tensor for a given flow is difficult and time consuming using traditional flow measurement techniques. However it is greatly simplified when the flow is measured at a high enough frequency and spatial resolution.

Glegg et al. ([2],[3], [4]) show that the sound of a rotor ingesting an anisotropic, inhomogenous turbulent shear flow can be accurately predicted for low and moderate thrust if the space-time correlation function of the upwash velocity at the rotor inlet is known. The correlation function is often estimated from single point statistics and Taylor's frozen flow hypothesis.

Turbulence stretching at the inflow to a rotating fan was discussed in Majumdar and Peake [5] and the stretching of the turbulence and its effect on flow lengthscales and subsequently the far field radiated noise is discussed. For static conditions the turbulence within the streamtube was strongly distorted due to the quiescent air surrounding the fan, allowing the fan thrust to more strongly distort the turbulence as it is ingested. However for inflight conditions the turbulence distortion is significantly weaker and the spectral humps were less prominent in the acoustic spectra. A similar study was conducted by Hanson [6] for a rotor in static conditions and significant stretching of the streamwise eddies was found; up to lengthscale ratio of 400:1 between the transverse and streamwise directions. These resulted in highly narrowband spectral humps within the acoustic spectra.

The purpose of the present study is to reveal the correlation structure of the turbulence, how it is influenced by angle of attack and stretching ahead of the rotor, and the impact those effects have on the far field sound. Measurements were performed using time resolved particle image velocimetry (PIV) and a far-field acoustic array for a range of rotor advance ratios. We present in the following section the details of the wind tunnel, body of revolution, rotor, and a description of the instrumentation. Results are then presented beginning with the acoustics and a brief description of the test conditions and orientation of the reader with the experimental setup. We then show the mean axial and circumferential pressures without the rotor spinning to confirm the angle of attack and describe the mean characteristics of the flow determined from the PIV. Diving further into the PIV data we examine the rotational phase averaged statistics of the flow to determine blade passage effects as well as examining correlated turbulence within the measurement plane. Finally the evolution of the two point correlation function along a streamline within the flow as it approaches and moves through the rotor inlet plane is examined. Comparisons of the two point correlation function between the 0°angle of attack, 5°pitch down angle of attack, and the 5°yaw starboard angle of attack cases are made.

II. Experimental Methods

A. Experimental Facility

The wind tunnel used to take the measurements is the Virginia Tech Stability Wind Tunnel (VTSWT) in anechoic configuration and is shown in Fig. 1. The 1.85 m x 1.85 m x 7.32 m test section is enclosed by two Kevlar side walls

and anechoic floor and ceiling panels. The freestream turbulence levels are less than 0.01% at 20 m/s and the mean flow has a freestream uniformity of 0.5% at 47 m/s [7]. Devenport et al. [8] goes into further detail of the VTSWT's capabilities. Fig. 1 shows the two orientations of the body of revolution as tested. A test section centered co-ordinate system is defined for use in locating the microphone array with respect to the BOR. Fig. 1 shows the origin of the test section centered co-ordinate system, X is positive downstream, Y is positive towards the test section ceiling, and Z is positive towards the port wall. The origin is located on the test section floor on the edge of the panel just upstream of the BOR nose and equidistant from the two Kevlar side walls.

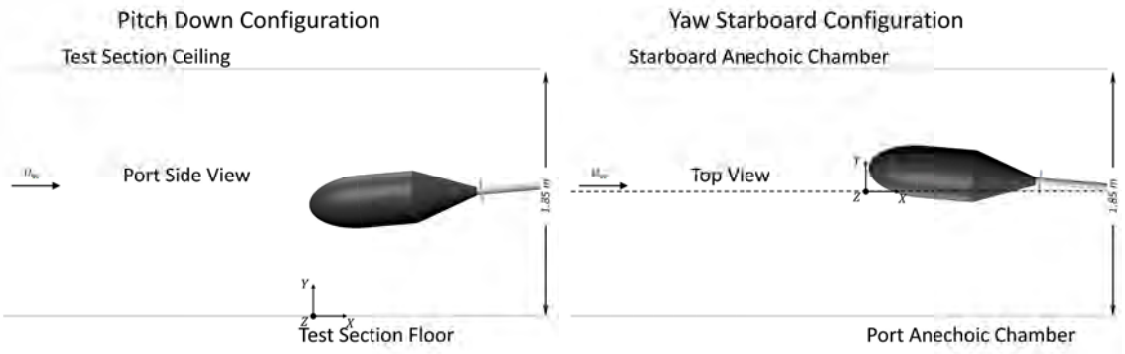

Fig. 1 Image of the body of revolution in the test section in the yaw starboard and pitch down configurations and with the relevant global test section co-ordinate system (X,Y,Z) shown.

B. Model

The non-axisymmetric flow was produced by a body of revolution pitched at a 5°angle of attack. It was tested in two configurations; pitch down and yaw starboard. The body of revolution in both configurations is shown in Fig. 1. It has a diameter of 432 mm and consists of three separate sections that produce specific flow phenomena. The nose is a 2:1 ellipsoid that produces a favorable pressure gradient as the fluid flows past it. The mid-body is a 432 mm diameter cylinder, and the aft section is a 1.17D long section with a 20°ramp to induce an adverse pressure gradient. The aft ramp narrows to a 50 mm diameter drive shaft on which the 216 mm diameter rotor is mounted. To ensure a turbulent boundary layer is grown over the length of the midbody, a 0.81 mm trip ring was placed at $x/D = 0.98$. A tether system consisting of 4x1/16" diameter wires were used to anchor the cantilevered body of revolution in place. The tethers are attached at $x/D = 1$ and extend to the corners of the test section. The effect of the tethers on the flow was examined in Balantrapu et al [9] and [10] and shown to have a non-negligible effect on the mean velocity and turbulence levels within the wake of the tether, however no effect was noted outside of the tether wake. The location of the tether's and effect on the cross-sectional mean flow structure at the rotor plane for zero angle of attack is shown in Fig. 2 courtesy of Balantrapu et al. [9]. The positioning of the body of revolution was measured to be within 0.2°of the targeted 5°angle of attack shown in Fig. 1.

The local co-ordinate system used for the BOR in the experimental test is a right-handed, body oriented system. The origin is centered on the BOR nose with x positive downstream, y positive vertically towards the test section ceiling, and z positive towards the port wall. The circumferential direction is defined positive clockwise with $\theta = 0°$on top of the BOR (from the perspective of an observer in the test section) in the 5°pitch down configuration. An illustration of the body oriented co-ordinate system is shown in Fig. 3.

The blockage area of the body of revolution within the test section is 4.3% and the location of the body of revolution and the rotor in each configuration with respect to the test section co-ordinate system is shown in Table 1. It should be noted that there is some slight asymmetry with regards to the location of the BOR within the test section. The test section center line is at $Y = 0.925$m and $Z = 0$m. In the 5°pitch down angle of attack the body of revolution is symmetrical about the $X - Y$ plane as we'd expect as the nose and rotor both lie at $Z = 0$. However there is some slight asymmetry about the $X - Z$ plane for the 5°yaw starboard plane as seen in the measurements for Y. Comparing Y values for the BOR nose and the rotor disc center we see that the BOR is both slightly pitch down and below the tunnel centerline by 25 mm.

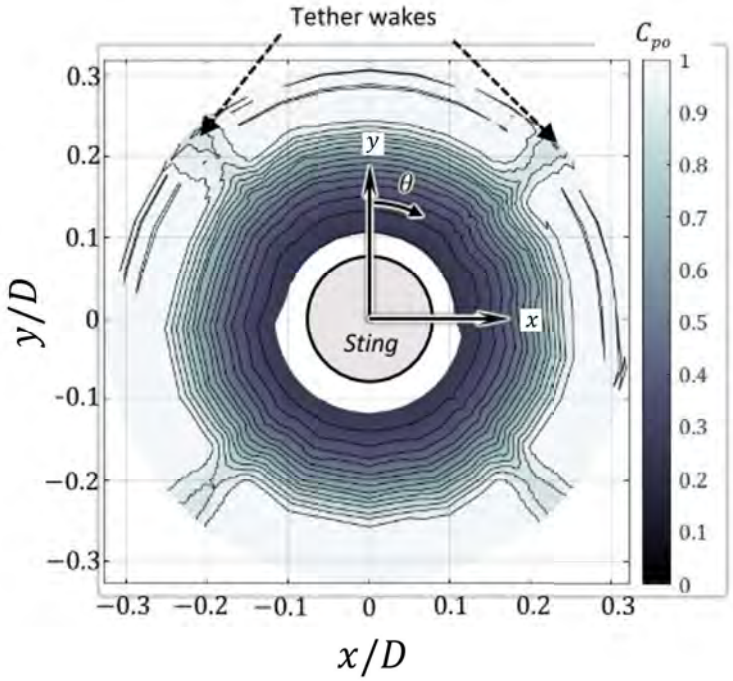

Fig. 2 Measurements of the stagnation pressure at the rotor inlet (x/D = 3.17) showing the effect of the tethers on the flow. The tethers are located at θ = 45°, 135°, 225°, and 315°. Plots are courtesy of Balantrapu et al. [9].

Configuration	Feature	X [m]	Y [m]	Z [m]
Pitch Down	BOR Nose	0.13	0.69	0.00
	Rotor Disc Center	1.32	0.83	0.00
Yaw Starboard	BOR Nose	0.12	0.89	-0.23
	Rotor Disc Center	1.28	0.90	-0.10

Table 1 Location of significant physical features of the BOR

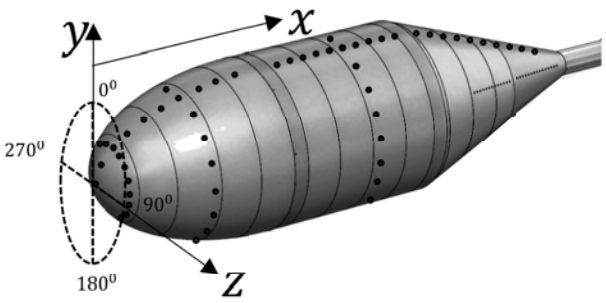

Fig. 3 Body centered co-ordinate system with the x-axis positive downstream, y-axis positive towards the test section ceiling, z-axis positive towards the port side wall. The circumferential co-ordinates are positive clockwise. Rotor is not shown but located at the aft end of the ramp.

C. Rotor

The rotor being used in this study is a custom 5-bladed rotor shown in Fig. 4. It is wake adapted for the axisymmetric wake produced by the body of revolution at 0°angle of attack. The rotor was designed for a zero thrust condition at an advance ratio of 1.44 in the 0°angle of attack configuration. The rotor has a diameter of 216 mm (D/2) and was sized so the blade span is completely engulfed by the boundary layer for the 0°angle of attack configuration. At 75% radius the blades have a maximum thickness of 6 mm, a pitch of 168 mm and a chord of 57 mm [9]. The rotor has no rake but has a 35.5°max sectional skew near the blade tip. Rotor scans were completed and determined that the rotor is axisymmetric to within 0.2 mm [11].

Fig. 4 CAD of the Zero-Thrust Rotor

D. Drive System

The rotor is mounted by a keyway onto a 50 mm shaft and driven by a Kollmorgen AKM54L-ACCNDA00 servo-motor with a 2.73 gear ratio. The shaft and rotor have a maximum rotation speed of 5000 rpm which limits the advance ratio to a maximum of about 1.27 at reference conditions ($Re_D = 600,000$). The drive system was faired with a 3D printed aerodynamic structure and acoustically treated with lead vinyl to reduce acoustic radiation from the motor and associated drive components. Fig. 5 shows an image of the rotor structure with the acoustic treatment installed. The upper structural components used to stiffen the rotor structure and reduce vibrations were faired with 3D printed NACA 0012 section airfoils and the lower structural components were faired with mylar airfoils. Overall blockage area of the drive system is about 7%. The drive system was positioned $1.6D$ downstream of the rotor.

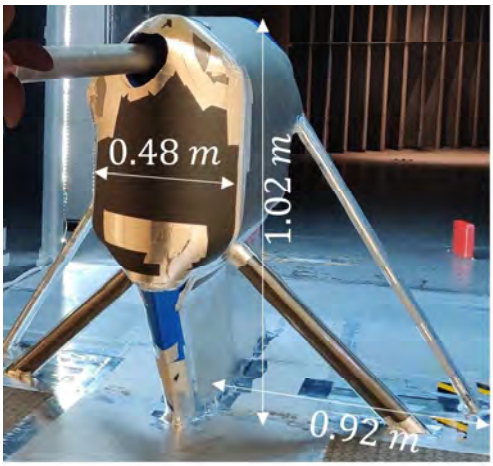

Fig. 5 Experimental photo showing the acoustic treatment applied to the drive system structure as well as principal dimensions and location of the drive system structure.

E. Acoustic Measurements

A 251-channel microphone array located in the starboard chamber was used for all acoustic measurements. This array was designed by AVEC, Inc and contains 251 GRAS 40PH-S5 1/4" microphones in four interlocking spirals

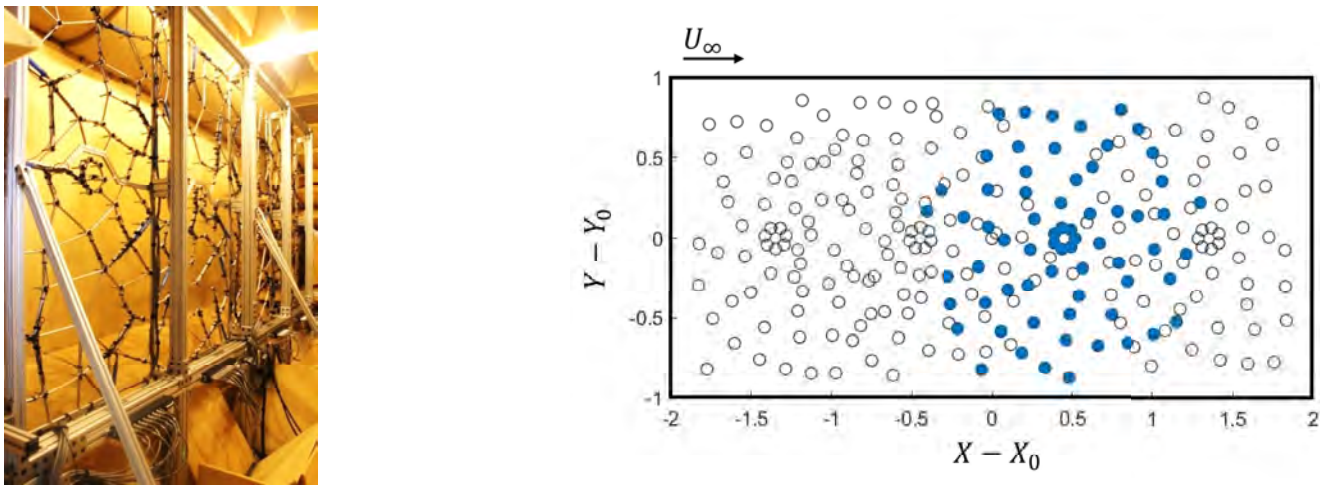

(a) (b)

Fig. 6 a) Image of the AVEC array from the starboard Kevlar chamber, b) 251 microphone array local coordinates, blue circles show Spiral 2. The center of the array in test section co-ordinates was measured to be $(X, Y, Z) = (0.4246, 0.866, 1.616)$**.**

shown in Fig. 6b. They have a dynamic range of 32-135 dB(A) and a sensitivity of 50 mV/Pa. This array allows for beamforming of sources within the test section and provides single-point measurements of the far field sound radiated by the model for cases with sufficient signal-to-noise ratios. The acoustic data shown in this paper was beamformed using a sub-array of the second most downstream spiral, denoted Spiral 2 (highlighted in blue in Fig. 6b) and then integrated over the rotor to determine the acoustic spectra. All beamformed data use diagonal removal and were corrected for convection and refraction. An image of the array is shown in Fig.6a. The center of the array given in the test section co-ordinates was measured to be $(X, Y, Z) = (0.4246, 0.866, 1.616)$m. From this location and the information in Table 1 the location of any of the microphones or individual spiral centers can be determined relative to the rotor location.

F. Particle Image Velocimetry

Particle Image Velocimetry was used to examine the velocity field at the aft end of the BOR. This setup gave three component velocity fields over a 160 x 160 mm^2 area with a 4.2 mm spatial resolution. The VTSWT is seeded by an MDG seeder that produces atomized Propylene Glycol particles on the order of one micron. The camera's used were Phantom v2512 high speed camera's with Nikon 200 mm lenses. The laser is a Photonic Industries DM laser with a maximum dual pulse rate of 12.848 kHz and a light sheet thickness of 2mm. The PIV was taken at the maximum sampling rate of 12.848 kHz in two frame mode to most accurately time resolve the flow. The length of each measurement was 1.87 s corresponding to between 144 and 168 rotations of the rotor corresponding to the lowest and highest rotor RPM. Fig. 7 shows the location of the laser light sheet, the camera viewing angles and the measurement plane in the 5°yaw starboard angle of attack configuration. The 5°pitch down angle of attack configuration has the same PIV setup except the camera angles and laser sheet have been moved to account for the change in location of the rotor inlet plane.

G. Phase Averaged PIV Analysis

The acquisition of the PIV was triggered cyclically by an optical RPM sensor placed on the shaft. PIV was triggered by the RPM sensor and images taken for a single rotation of the rotor, when the RPM sensor is triggered again by the full rotation of the shaft a second cycle of recording is started. Each cycle is stored as a subset of f_s/Ω images and this process continues up to a maximum of $24,000$ images. Phase averaged statistics can be computed from these data sets by averaging over all cycles at each image. The PIV for the pitch down J=1.44 condition consisted of 172 images repeated 131 times. This gives 172 positions, or phases, of the rotor with 131 samples of each phase. These samples were averaged to find a phase average that was a function of the blade position for one rotor rotation. For the pitch down plane there are 35 images between each blade passage indicating each phase corresponds to a rotation angle of

Fig. 7 Experimental photo showing the location of the PIV measurement plane and the laser and camera location setup for the 5°yaw starboard angle of attack configuration.

$\theta = 2.06°$. For the yaw starboard J=1.44 case the data set consisted of 168 images repeated 147 times. There are 34 images between each blade passage indicating each phase corresponds to a rotation angle of $\theta = 2.12°$. Radial profiles at $x/D = 3.17$ of the mean velocity and Reynolds Stress as a function of the rotor position, or phase, were extracted from the time resolved PIV for the two 5°angle of attack configurations and shown in Section IV.A.

H. Single and Two Point Correlation Functions

Inputs to many turbulent ingestion noise models include the axial and azimuthal integral length scale of the flow. Experimentally these have been traditionally estimated using the integral time scales from single point statistics measured using techniques such as hotwire anemometry or laser Doppler anemometry. This can be done by assuming Taylor's frozen flow hypothesis; that the turbulence within the flow is frozen and convected along at a constant convection velocity, U_c. In general this convection velocity has been found to be approximately the local mean velocity. This finding falls off once the boundary layer moves into the inner region and large scale effects diminish [12]. The single point correlation function can be found using the equation below,

$$\rho_{u_s u_s}(x, y; \Delta x_s) = \frac{\langle u_s(x', y') u_s(x', y', x' - U_s\tau)\rangle}{\sqrt{\langle u_s(x', y')^2\rangle \langle u_s(x', y', x' - U_s\tau)^2\rangle}} \tag{1}$$

The time-scale can be found by integrating the correlation function,

$$\Gamma_{u_s}(x, y) = \int_0^\infty \rho_{u_s u_s}(x, y, \tau) d\tau \tag{2}$$

and the length scales associated with the frozen flow assumption become,

$$L_{st}(x, y) = \Gamma_{u_s}(x, y) U_s \tag{3}$$

However with the PIV data available we have the full time resolved velocity field (spatially resolved to 4.2 mm) and the full four dimensional space-time correlation function of the turbulence can be computed and analysed. The results for this correlation function will be shown for various thrusting conditions. The two point correlation function of the streamwise velocity within the rotor plane will also be examined and compared to the previous axisymmetric test [13].

The two point correlation function referred to in this text is a spatially defined correlation of the velocity values in the streamwise direction. The two point correlation can be written mathematically as detailed in Pope [14],

$$\rho_{u_s u_s}(x, y) = \frac{\langle u_s(x, y) u_s(x', y') \rangle}{\sqrt{\langle u_s^2(x, y) \rangle \langle u_s^2(x', y') \rangle}} \tag{4}$$

Application of this formula involves selecting an anchor point (x, y) and then computing the correlations between the anchor point and all other points in the measurement plane, denoted by (x', y'). This correlation is then normalized on the variance such that the maximum value of the two point correlation occurs where $(x', y') = (x, y)$ and is equal to 1. The associated length scales of the flow are computed from this two point correlation function by integrating along the flow direction in the following manner,

$$L_s(x, y) = \int_0^\infty \rho_{u_s u_s}(x, y) ds \tag{5}$$

III. Results

A. Acoustic Measurements

Acoustic measurements were made using the AVEC 251-microphone phased array described in Section II.E. The data were beamformed using Spiral 2 and conventional delay and sum beamforming and then integrated over the rotor regions for both pitch down and yaw starboard cases. The data were processed with a record length of 8192 samples and were sampled at 51.2 kHz. The cross-spectral matrix was computed using a Hanning window with 50% overlap resulting in 400 windows which were then averaged. The view of the rotor from the center of Spiral 2 is shown in Fig. 8. Fig. 9 shows a comparison of the acoustic spectra between 0°angle of attack, 5°pitch down angle of attack, and 5°yaw starboard angle of attack at zero thrust. The horizontal axis shows frequency normalized on the blade passage frequency (BPF) and the vertical axis shows the noise spectra in SPL normalized on the square of the freestream and the blade relative velocity cube. The red curve shows the 0°case as examined in Hickling et al. [9], the blue curve shows the 5°pitch down case, and the green curve shows the 5°yaw starboard case. Examining Fig. 9 the 5°yaw starboard case is consistently seen to be about 5 dB louder than the 0°and the 5°pitch down case. Banks et al. [15] explained the differences seen in Fig. 9 using rotor directivity and the overall TKE levels seen in the RANS calculattions of the flow over the body without a rotor, performed at the University of Notre Dame (Dr's Di Zhou, M. Wang, private communication). Due to rotor directivity, much of the contribution to the overall radiated noise comes from the turbulence cut by the blade when it is at $\theta = 180°$(ie. beneath the tail of the body from the perspective of an observer in the test section in either pitch down or yaw starboard orientation). In the 5°yaw starboard case the rotor is cutting the most turbulent region of the flow when $\theta = 180°$.

Noise levels decrease with an increase in frequency and haystacks are seen at multiples of the BPF's in all thrust cases with the intensity of the haystacks increasing with thrust. The haystacks are caused by blade to blade correlation of turbulent structures within the flow, indicating that as the thrust increases successive blades are cutting the same turbulent structures multiple times. The turbulence intensity of the flow affects the broadband levels of the radiated noise, and the length scales of the flow are directly related to the extent of the haystacking seen in the acoustic spectra. The effects of the body of revolution's non-axisymmetric flow field on both of these quantities is discussed in later sections of the paper by examining the two point correlation function and turbulence levels within the two PIV planes.

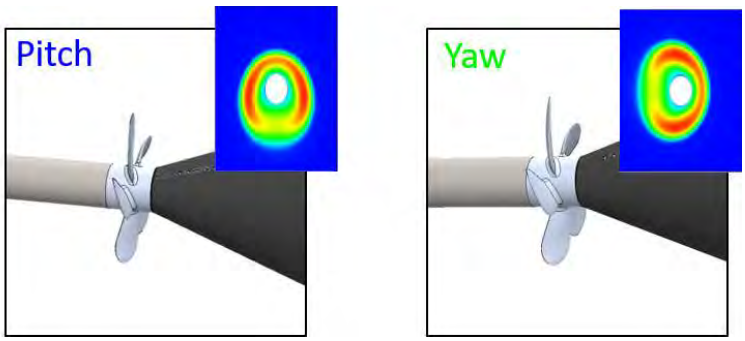

Fig. 8 3D model showing the orientation of the rotor with respect to spiral 2 of the AVEC array for 5°pitch down angle of attack and 5°yaw starboard angle of attack. RANS simulations performed at UND (Drs Di Zhou, M. Wang, private communication) characterize the circumferential variation of the turbulent kinetic energy on the top right of each image.

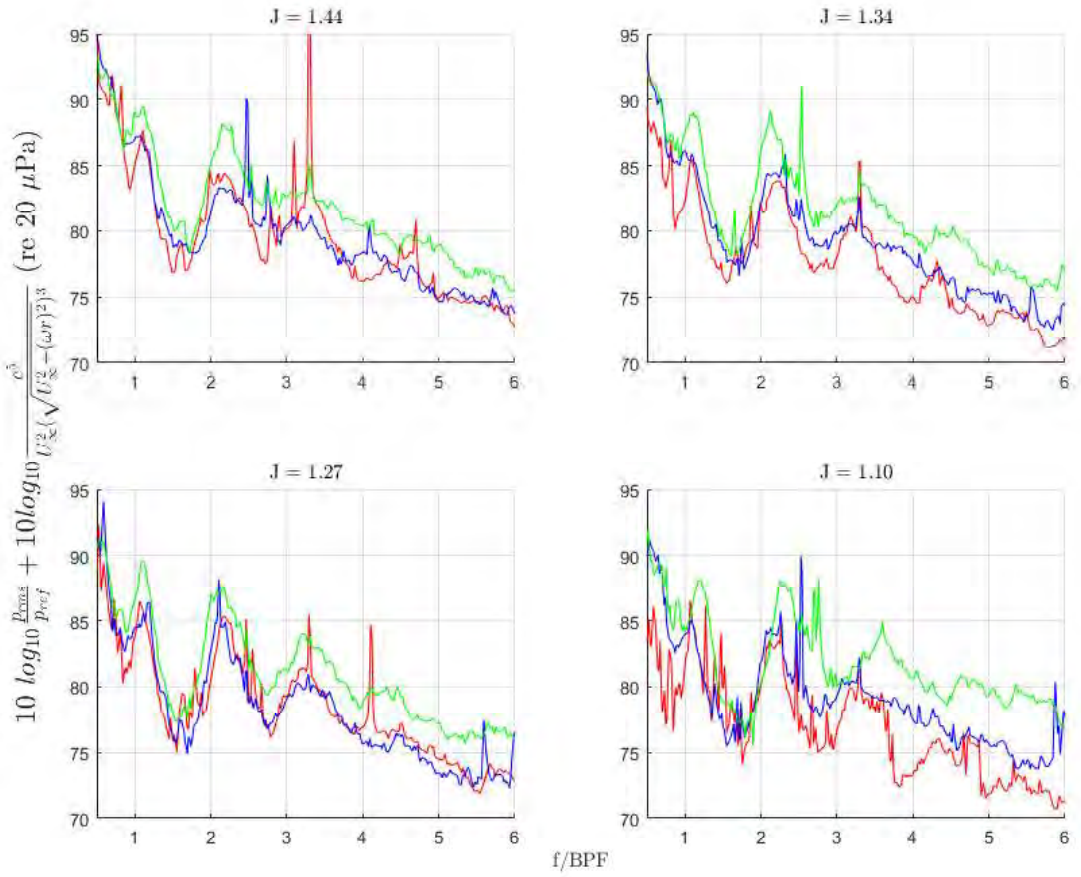

Fig. 9 Acoustic noise measured by the AVEC array for several advance ratios from the perspectives shown in Fig. 8. The red line in each case is the 0°angle of attack, the blue line is the 5°pitch down case, and the green line is the 5°yaw starboard case. The horizontal frequency scale is normalized on the blade passage frequency and shown up to 6 multiples of the BPF.

B. Test Conditions and Measurement Locations

Most tests were run at a body diameter based Reynolds number of $600,000 \pm 2,000$. Accounting for temperature variations throughout the test campaign this resulted in tunnel freestream speeds of between 19 and 24 m/s for the various advance ratio's measured. The maximum shaft speed of 5000 rpm limited the ability of the rotor to operate at high thrusting conditions so for advance ratios lower than $J = 1.27$ the Reynolds number was dropped to $500,000$. The lowest advance ratio examined in this paper is $J = 1.10$ and the conditions for each advance ratio are shown in Table 2 below.

Table 2 Advance ratios, Reynolds numbers, and Mach Numbers for PIV measurements

Advance Ratio, J	Re_D	Freestream Mach Number
1.10	500,000 ± 2,000	0.0571 ± 0.014
1.44, 1.34, 1.27	600,000 ± 2,000	0.0698 ± 0.0038

The PIV measurements were taken at two streamwise oriented locations underneath (as seen in Fig. 10c) the BOR. Figs. 10a and 10b below are experimental photos of the body of revolution at two angles of attack, pitch down 5°and yaw starboard 5°. Figs 11a and 11b below are RANS simulation of the turbulent kinetic energy corresponding to the two experimental configurations of the body of revolution. These calculations were done by Dr Di Zhou at the University of Notre Dame and demonstrate the circumferential variation of the flow. It indicates that the turbulent kinetic energy is a function of the circumferential location around the BOR, in the lee of the body ($\theta = 180°$in the 5°pitch down angle of attack) the turbulence is greatly reduced. By changing the experimental configuration between pitch down and yaw starboard but keeping the PIV measurement plane in the same location ($\theta = 180°$in the body fixed co-ordinate system) two different cross sections of the flow around the body of revolution are being quantified. In the pitch down configuration this corresponds to the plane on the lee side of the body which is the least energetic part of the flow (see Fig. 11a) and in the yaw starboard configuration it corresponds to the peak turbulent kinetic energy (see Fig. 11b). For both cases the measurement plane is taken at $\theta = 180°$, $z/D = 0$ and extends upstream of the rotor plane to $x/D = 2.9$ and downstream of the rotor plane to $x/D = 3.2$, giving a total streamwise measurement length of approximately 132 mm. The measurement plane extends spanwise from $y/D = -0.15$ to $y/D = -0.4$ approximately 150 mm.

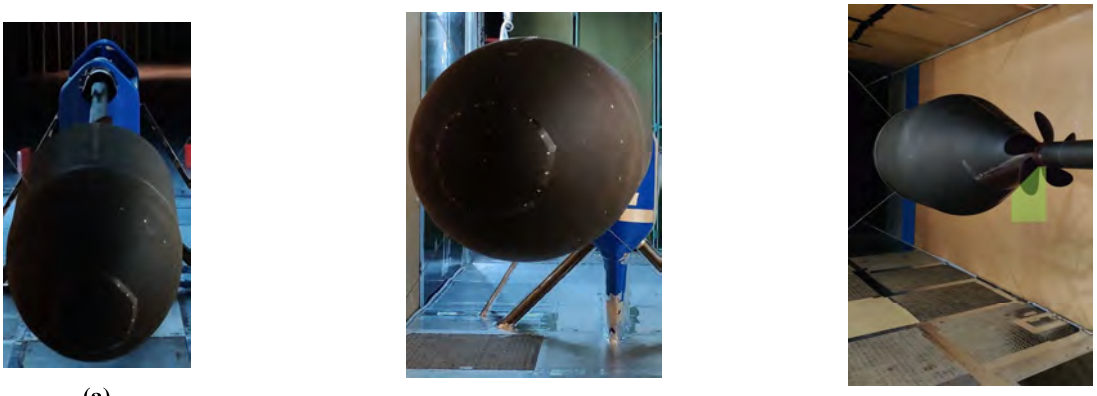

(a) **(b)** **(c)**

Fig. 10 Experimental setup photos showing the body of revolution in a) 5°pitch down angle of attack looking downstream, b) 5°yaw starboard angle of attack looking downstream, c) location of the rotor relative to the body of revolution in 5°yaw starboard angle of attack looking upstream with the array behind the kevlar wall on the right and the measured PIV plane illustrated in green

C. Pressure Distribution

The mean axial and circumferential pressures were measured using static pressure ports in various positions on the body of revolution. The axial pressure variation was measured by pressure ports distributed along the length of the body of revolution from the nose ($x/D = 0$) to the end of the tail cone ($x/D = 3.1717$) at $\theta = 0°$of the body of revolution.

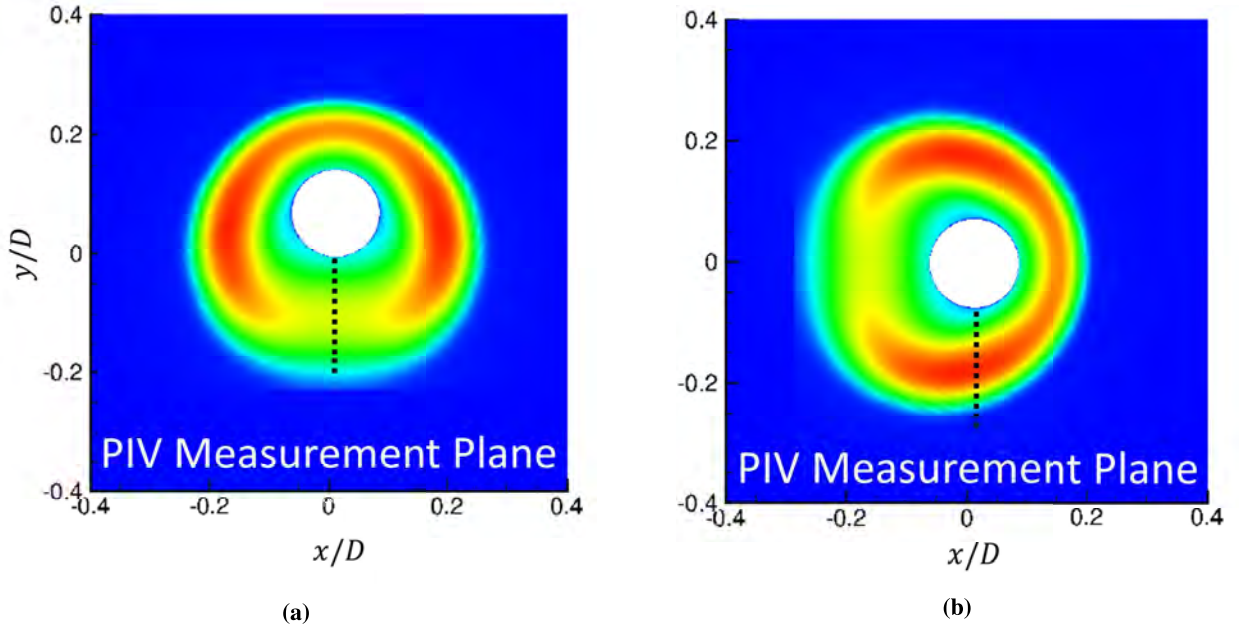

Fig. 11 RANS simulation of the circumferential variation of the turbulent kinetic energy around the body of revolution at angle of attack at the rotor plane ($x/D = 3.17$). The RANS calculations were performed at the University of Notre Dame. a) pitch down turbulent kinetic energy, b) yaw starboard turbulent kinetic energy.

The circumferential ports were distributed in two rings around the nose of the body of revolution at $x/D = 0.095$ and $x/D = 0.5$. The measurements shown are for the $x/D = 0.5$ circumferential location. Fig. 12a shows the coefficient of pressure on the vertical axis as a function of the downstream distance from the body of revolution nose normalized on the body diameter for rotor off condition. The axial pressure distribution shows the variation in the body pressure for the two different experimental configurations. Similar to the quantification of different flow fields described in Section III.B the axial pressure measures the pressure distribution along a body centered plane at $\theta = 0°$for both configurations but captures different pressure distributions due to the body orientation change.

The axial pressure drops from close to 1 at the nose reaching a shallow minmimum just upstream of the trip near $x/D = 1$. As it passes over the corner of the aft ramp the pressure drops precipitously to a minimum at the ramp corner before rising again just as quickly. It is evident that the nose produces a favourable pressure gradient and the aft ramp produces a strong adverse pressure gradient near the aft ramp corner with the pressure gradient continuing to be adverse up until the rotor inlet.

The pressure distribution was also used to confirm the body of revolution's angle of attack. The tethers were iteratively adjusted and the pressure distribution in the circumferential location was compared to the RANS results to ensure the aerodynamic angle of attack matched the RANS results. The corresponding angles for yaw starboard were rotated anti-clockwise 90°to properly compare the flow to the pitch down case. The 90°rotation used to compare the two circumferential pressure distributions means the windward side appears at $\theta = 180°$in both cases. On the windward side of the body the pressure is highest at a $C_p = 0.45$ and decreases monotonically and symmetrically to a C_p of 0.23. The difference between the C_p values of the 5°pitch down angle of attack and the 5°yaw starboard angle of attack is at most 0.1 and occurs on the lee side of the body. The excellent agreement between the RANS results for both the axial and circumferential distribution demonstrate that the aerodynamic angle of attack is 5°±0.2°in both experimental configurations.

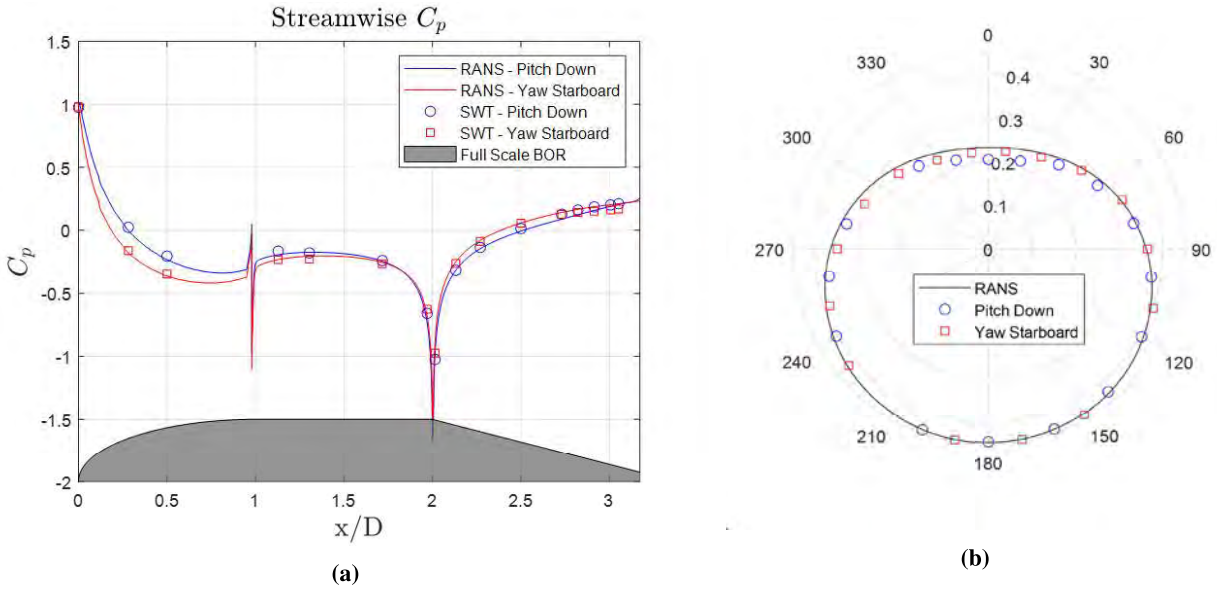

(a) (b)

Fig. 12 Pressure distribution on the body of revolution with rotor off a) shows the axial distribution with C_p on the y-axis, and streamwise distance on the x-axis, b) shows the circumferential distribution of the pressure for the body at angle of attack.

D. Mean Flow and Boundary Layer Characteristics

Contours of the mean flow for the zero thrust condition ($J = 1.44$) for the 0°angle of attack, 5°pitch down angle of attack, and 5°yaw starboard angle of attack are shown in Fig. 13. The boundary layer edge is defined as the point at which the turbulence intensity drops below 1.5% ie. $\sqrt{\overline{u_x^2}/U_\infty^2} < 0.015$ and is indicated by a thick black line. For the 5°pitch down case (Fig. 13b), where the measured plane is in the lee side of the body, the boundary layer is thicker than that seen at 0°angle of attack (Fig. 13a) and grows at roughly the same rate as the taper of the body tail. While the boundary layer appears quite low momentum, with measured velocities as low as 0.2 U_∞ being reached within $0.03D$ from the tail and rotor shaft surface, there is no evidence of mean flow separation. The deflection of the streamlines as they pass through the rotor plane is clearly visible. In the yawed configuration (Fig. 13c) where the PIV is sensing the flow as it sweeps from the windward to leeward sides, the boundary layer is much thinner and the shear much more concentrated within about 75% of the blade radius from the BOR surface. Surprisingly, mean velocities closest to the body surface are actually lower than on the lee side, suggesting that we may be looking at a cut through a three dimensional shear layer in the process of separating from the body surface. Indeed, this is suggested by the RANS results of Fig. 11. Moving on to the streamwise turbulence stresses shown in Fig. 14 the 5°yaw starboard angle of attack case confirms the shear layer concentration at around 75% blade radius with turbulence levels shown in Fig. 15 to be almost twice that of the 0°case. Turbulence values in the 5°pitch down angle of attack case are significantly depressed when compared to both the 0°and the 5°yaws starboard case. Examining Fig. 11 the flow imaged in Figs. 13b occurs in the least energetic area of the flow where the levels of TKE are lowest, whereas that in the 5°yaw starboard case occurs at the highest levels of TKE. Recalling the discussion regarding rotor directivity in Section III.A the high turbulence shear layer seen here in the mean turbulence contours shows confirmation between the RANS results and the PIV and helps explain Fig. 9.

Fig. 15 shows a comparison of turbulence profiles at the rotor inlet for the 3 cases. The vertical axis shows absolute distance from the co-ordinate system axis normalized on y/D and the horizontal axis shows the levels of turbulence normalized on the square of the free stream. Hickling [11] showed that the peak turbulence of $\overline{u_x^2}/U_\infty^2 = 4\text{x}10^{-3}$ for the 0°angle of attack configuration occurs at approximately 75% of the blade radius. In comparison the data for the pitch down show the peak turbulence of $\overline{u_x^2}/U_\infty^2 = 2.8\text{x}10^{-3}$ occurring at approximately 50% of the blade radius with a secondary, lower intensity peak at 75% blade radius, and a further, lower intensity peak at 100% blade radius. The nature of the triple peak for the pitch down case in the Reynolds stress was discussed in Banks et al. [15]. The yaw starboard Reynolds stress shows strong evidence of a turbulence peak centred at 75% of the blade radius. This more

strongly matches what was seen in Hickling's [11] data, however the turbulence levels are approximately twice that seen in the 0°case. Comparison of the low turbulence values for the pitch down case and the significantly higher turbulence values for the yaw starboard case shows evidence of the non-axisymmetry of the inclined BOR.

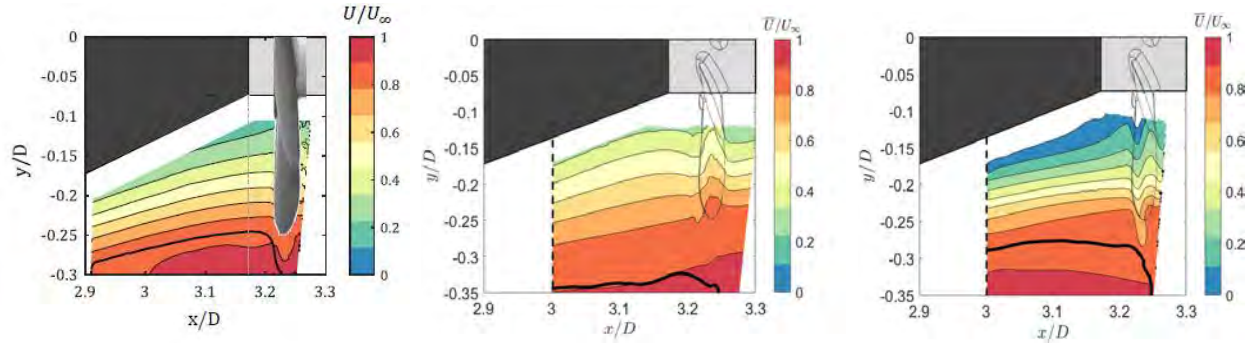

(a) (b) (c)

Fig. 13 Contours of the mean velocity in the x-direction for the three body of revolution configurations at $J = 1.44$. a) 0°angle of attack, b) 5°pitch down angle of attack, c) 5°yaw starboard angle of attack. The solid line shows the boundary layer thickness and the dotted lines show the location of the radial profiles taken for Section IV.A.

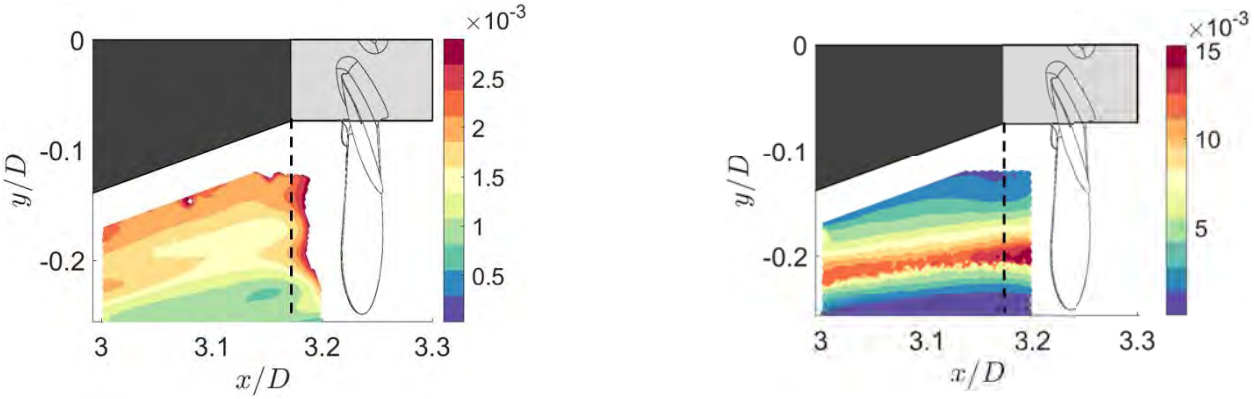

(a) (b)

Fig. 14 Contours of the average Reynolds Stress in the streamwise direction normalized on the square of the freestream ($\overline{u_x^2}/U_\infty^2$) for a) pitch down 5°angle of attack and b) yaw starboard 5°angle of attack with the rotor inlet plane shown as dotted line.

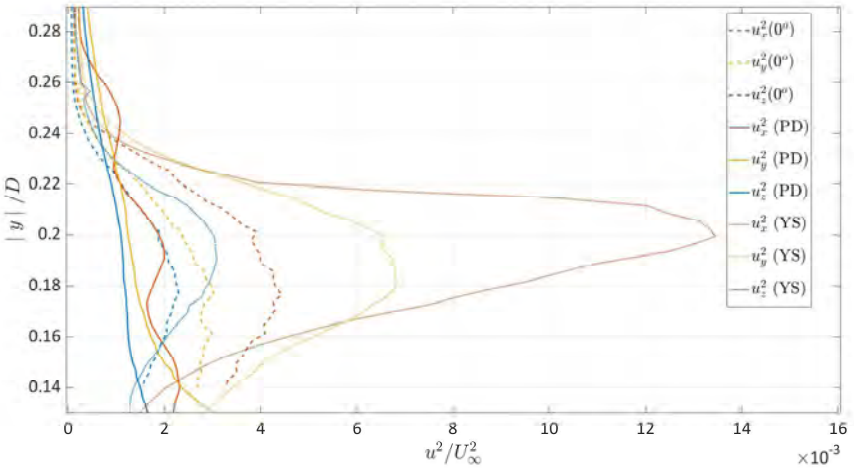

Fig. 15 Average turbulence profiles taken at the rotor inlet plane shown in Fig. 14 comparing the 3 different body of revolution configurations, turbulence levels are shown on the x-axis and are normalized on the square of the freestream, and the vertical distance is shown on the y-axis. PD - pitch down 5°, YS - yaw starboard 5°

IV. Phase Averaged Results

A. Radial Profiles of the Phase Averaged Mean Velocity and Reynolds Stress

Figs. 16a and 16c show the average fluid velocity seen by each phase of the rotor as it moves through the PIV measurement plane. These plots are generated using the approach detailed in Section II.G so any structures or variation within the flow occur at the same phase in every image and they are then phase correlated features. The effect of the rotor is seen in the pentagonal shape of Fig. 16a and 16c. The five bladed rotor accelerates the flow at each blade passage so a local acceleration of the flow is seen as the blade passes, this corresponds to the flat sections within the radial profile plots (Figs. 16a and 16c). The bulging lobes in the phase averaged velocity profiles are phases with relatively slower velocities when compared to the flat sections. They occur between blade passages and show the absence of the rotor blade at that position of the rotation. The rotor passage effect is more prominent in the mean velocities for the 5°pitch down angle of attack when compared to the 5 °yaw starboard angle of attack. We can explain this by examining the overall turbulent energy within the flow at the rotor inlet for the two cases. Recalling Fig. 15 the maximum $\overline{u_x^2}/U_\infty^2$ within the flow for the pitch down case is on the order of $2\text{x}10^{-3}$, whereas for the yaw starboard case it is on the order of $1.5\text{x}10^{-2}$, almost an order of magnitude difference. The rotor is designed to have zero thrust at $J = 1.44$ so we should expect minimal flow acceleration effects at this condition. However the low energy plane at $\theta = 180°$in the pitch down configuration results in a piece of the flow in which the rotor has a non-zero thrust and we see rotor effects in both the mean flow and the turbulence.

The phase averaged turbulence stress contours show both expected and unexpected features. For the measurements made in yaw, Fig. 16d, the contour map reveals what appears to be a shear layer with features that appear statistically almost identical regardless of blade phase. Surprisingly this is not true for the measurements made on the lee side (Fig. 16b) the contours show the much thicker, weaker, turbulent region revealed in the mean profiles, but we see that the thickness of this region varies with blade rotation, resulting in the same pentagonal overall form seen in the phase averaged mean velocities (see the red region within Fig. 16b). Most interesting of all there is evidence of phase correlated turbulence within the radial turbulence profiles for the 5°pitch down case that is not seen in the 5°yaw starboard case. These are evident as circumferential structures that start at a specific point in the profile and sweep circumferentially and radially such that they trace an arc through the plane in the same manner as the blade. Further analyses of these structures for higher thrusting cases are shown in Fig. 17 below and discussed in the following paragraph.

This irregular phase averaged structure on the lee side of the BOR is also seen further upstream of the rotor, and appears more intense if the advance ratio is reduced. This is shown in Figs 17a and 17b where radial profiles at $x/D = 3.00$ are shown. This location is shown in Fig 13b. At J=1.44 (Fig 17a) the radial profiles show evidence of repeating helical structures at approximately 130% blade radius. These features become much more intense as the

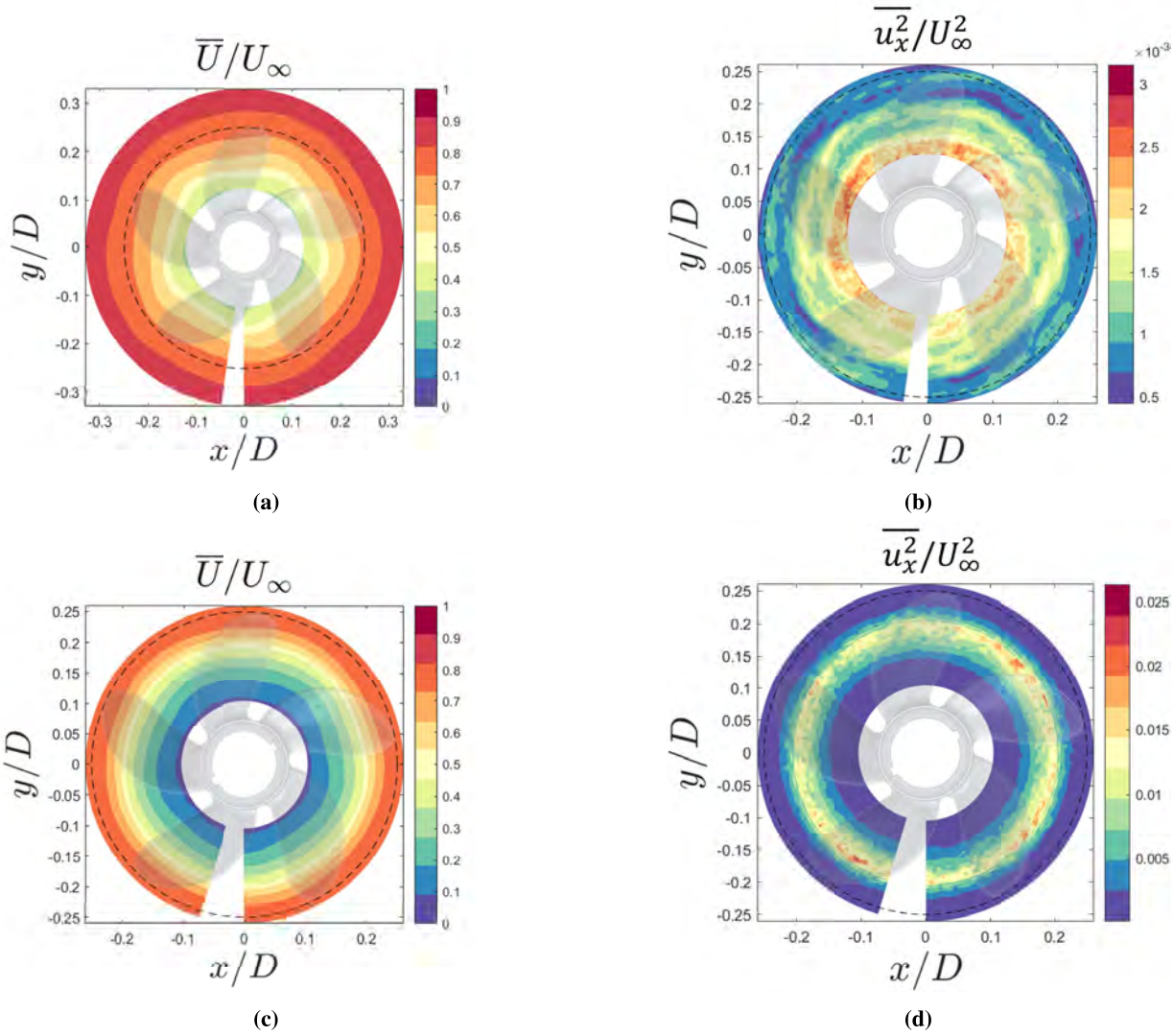

Fig. 16 Contours of the radial profiles of the mean velocity in the x-direction and the Reynolds stress as a function of rotor phase at the rotor inlet for the two different non-axisymmetric configuration at $J = 1.44$: a) pitch down mean velocity, b) pitch down Reynolds stress, c) yaw starboard mean velocity, d) yaw starboard Reynolds stress. The rotor blade position is shown overlaid over the data and the dotted line shows the rotor diameter.

advance ratio is reduced to J=1.27 (Fig. 17b) and we can identify them repeating 6 times per rotation. The strongest structures peak at $\overline{u_x^2}/U_\infty^2 = 6\text{x}10^{-4}$ and repeat approximately every 54°corresponding to a frequency of 566 Hz. Examining Fig. 17b it is evident that there are 3 strong structures in the lower quadrants, a single strong structure in the upper right quadrant and 2 weaker structures in the upper left quadrant of the radial profiles. In order to better illustrate the convection of these structures the entire phase averaged flow field for the $\overline{u_x^2}/U_\infty^2$ is shown for 9 profiles indicated by the dotted lines on Fig. 17b. Within the flow field in Fig. 18 we see several regions of higher intensity turbulence convecting downstream with the flow. These extend from $y/D = -0.31$ to $y/D = -0.37$ and are angled 17°clockwise from the horizontal. These phase correlated turbulent structures appear to convect downstream with time and dissipate somewhat as they move downstream. The effect these have on the acoustics is likely to be broadband, centred on the BPF and harmonics. They repeat predictably with phase and are therefore blade correlated but are not visible with the phase averaged velocity and we don't see them show up sufficiently within the acoustic spectra to identify them. For the case of this rotor and the advance ratios tested their turbulence intensity is simply too low for them to be heard relative to the other parts of the flow. It will be interesting to identify if these structures contribute significantly to turbulence

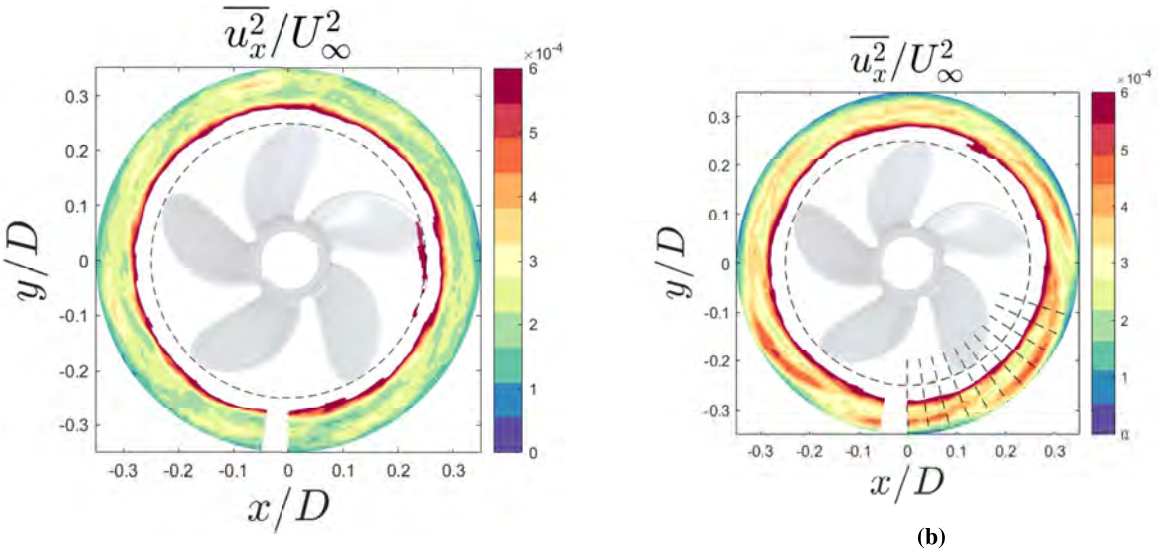

Fig. 17 Phase averaged Reynolds stress $\overline{u_x^2}/U_\infty^2$ for a single rotation for an advance ratio of a) J=1.44, b) J=1.27, a single blade passage is $360/5 = 72°$. Data is taken for the 5°pitch down case. The dotted lines on b) indicate where snapshots of the full flow are taken for Fig. 18

ingestion noise in higher thrusting rotors for future tests.

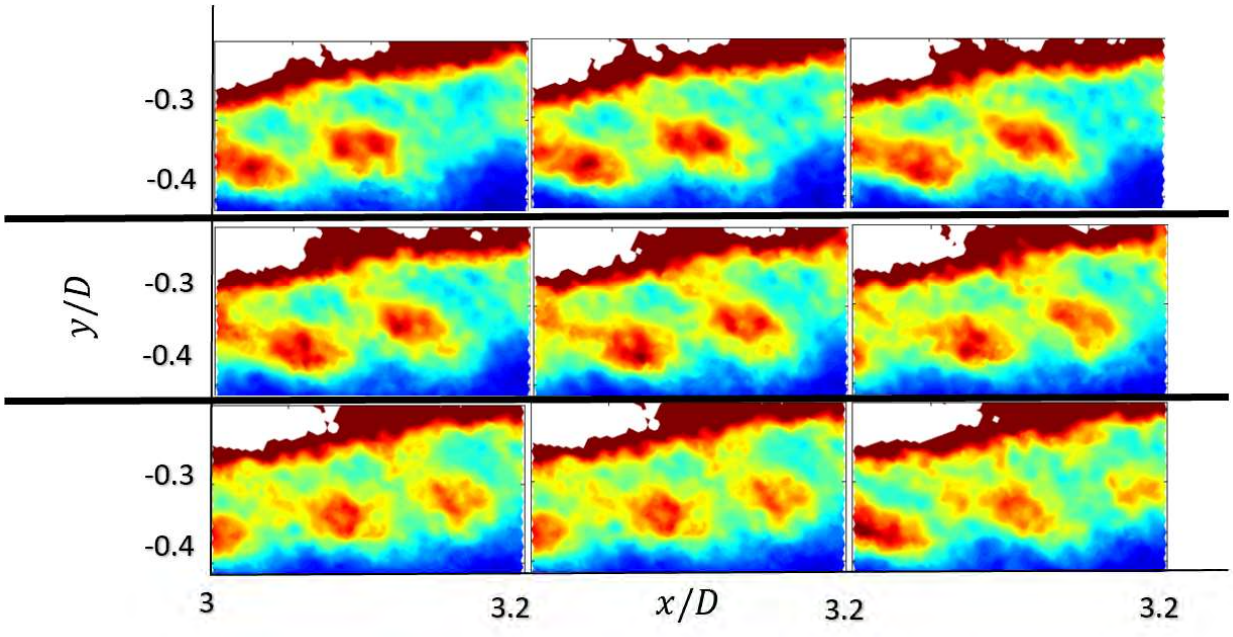

Fig. 18

Fig. 19 Snapshots from 0°to 57.6°taken from Fig. 17b at the indicated dotted lines showing repeated, phase averaged, convected structures.

V. Correlation Structure

A. Two Point Correlation Structure in the Rotor Plane

The correlations developed in this section correspond to the zero thrust condition ($J = 1.44$) at 0°angle of attack, 5°pitch down angle of attack, and 5°yaw starboard angle of attack. Fig. 20 shows the correlation structure at the rotor inlet for both these conditions. The two point correlations shown in Fig. 20 are computed using all images in the PIV data set for each configuration using the mathematics described in Section II.H and directly use Eq. 4. The anchor point for these comparisons was chosen to be $(x, y) = (3.17, -0.2)$ which corresponds to 0.5δ for the 0°case and is within the high turbulence shear layer for the 5°yaw starboard case. The two point correlation function is normalized on the variance and gives a maximum correlation value of 1 at $(x, y) = (3.17, -0.2)$, this value decays as a function of distance from the anchor point. The rapidity of its radial decay defines the two point correlation function and gives insight into the stretching of the flow lengthscales as a function of space. The correlation structure for the 0°angle of attack case is stretched in the streamwise direction ($L_s/L_sp \approx 4.5$) and the major axis is rotated 18°clockwise from the BOR x-axis. Comparing the turbulence structure for the 0°angle of attack configuration in Fig. 20a to the data shown in Figs. 20b and20c there is an increase in the rotation of the correlation structure but a decrease in stretching, with the pitch down configuration showing the greatest rotation at 18°, followed by the yaw starboard configuration at 16°. Comparing the stretching between the 3 cases the 0°case has the greatest ratio of lengthscales with ($L_s/L_sp \approx 4.5$) followed by the 5°pitch down case at $L_s/L_sp \approx 2.6$ and then the yaw starboard case with $L_s/L_sp \approx 1.8$. The effect this has on the acoustics is related to the haystacking within the spectra for higher thrusting cases. Increasing the streamwise to spanwise length scales (L_s/L_sp) will act to increase the extent to which haystacking occurs within the acoustic spectra as blade to blade correlations increase.

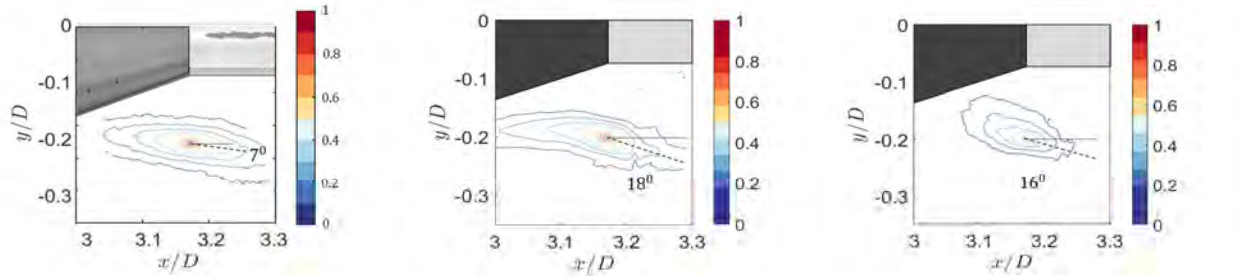

(a) **(b)** **(c)**

Fig. 20 Two point correlation functions computed from the PIV results at the rotor inlet and approximately halfway into the boundary layer. a) 0°angle of attack, b) 5°pitch down angle of attack, c) 5°yaw starboard angle of attack.

B. Two Point Correlation Structure Along a Streamline

The evolution of the two point correlation function within the flow was examined by taking a streamline and calculating the full structure of the two point correlation at 8 points along the streamline. Fig 21a and 21b show contours of the mean Reynolds stress in the x-direction ($\overline{u_x^2}/U_\infty^2$) within the rotor inflow plane. The horizontal axis shows the x-axis and the vertical axis shows the y-axis as defined in Fig. 1 as well as the streamline with the anchor points for the two point correlations marked. The start points for the streamlines were chosen such that the streamline passed through the rotor disc at approximately 75% of the rotor diameter. In both configurations, as the two point correlation moves along the streamline it stretches in the streamwise direction. In the pitch down case the major axis is rotated clockwise as it evolves, however this rotation is less evident in the yaw starboard case. The effect of the rotor on the two point correlation is seen in the two point correlations for anchor points 6,7, and 8 in the 5°pitch down case. The tail of the correlation function stretches significantly through the rotor. The rotor effect on the 5°yaw starboard case is less evident. The differences between the rotor's effect on the two-point correlation for the two cases is likely due to the turbulence intensity within each streamline. In the 5°pitch down case the turbulence values $\overline{u_x^2}/U_\infty^2$ are on the order of $1\text{x}10^{-3}$ whereas in the 5 °yaw starboard case the turbulence values are on the order of $14\text{x}10^{-3}$. The large difference between these two cases implies that the discrepancy is likely due to turbulence effects dominating the flow in the 5°yaw starboard case, and rotor effects being more prominent in the 5°pitch down case.

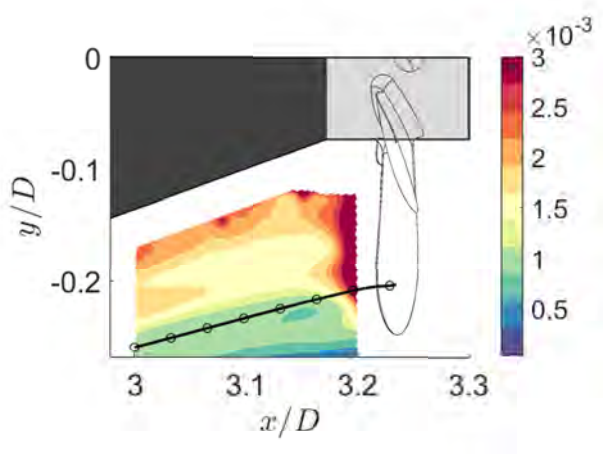

(a) Pitch Down Anchor Points

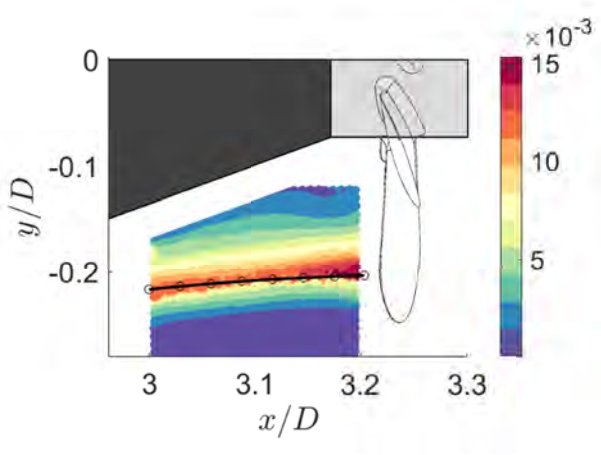

(b) Yaw Starboard Anchor Points

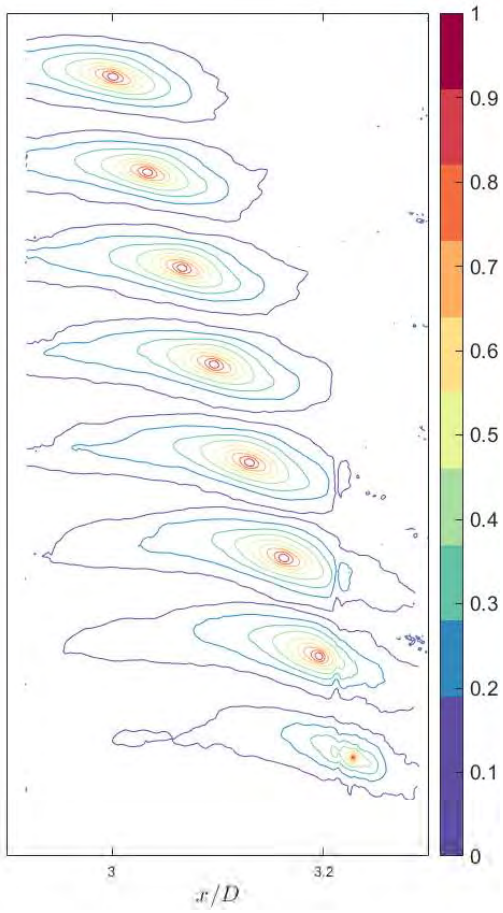

(c) Pitch Down Correlation Functions

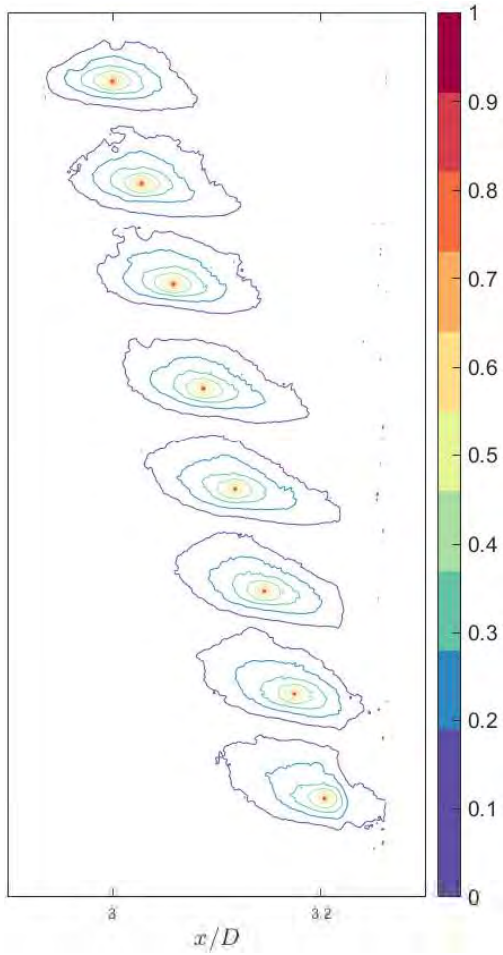

(d) Yaw Starboard Correlation Functions

Fig. 21 a) and b) show the anchor points along the streamline for the two point correlation calculations in c) and d). c) and d) show contours of the evolution of the two point correlation function. The x-axis shows streamwise distance normalized on the body diameter. The y-values for the correlation function where manipulated to obtain separation to illustrate the evolution effectively.

VI. Conclusion

Several measurements of the flow around a body of rotation inclined at an angle of attack with a rotor at the rear were taken. The axial and circumferential mean pressure distribution was shown to match the RANS calculations of the inclined body, indicating the aerodynamic angle of attack was within 0.2°of 5°. Microphone array measurements were taken for several advance ratios and the resultant spectra plotted for the two different configurations. The analysis of time resolved particle image velocimetry taken at a plane at $\theta = 180°$in the body centered co-ordinate system of the two configurations captured two pieces of the flow. Comparisons between the 0°configuration and the 5°configurations show that for the 5°pitch down angle of attack case the turbulence is significantly depressed and doesn't exhibit the typical peak turbulence behaviour expected of axisymmetric flow. For the PIV plane measured in the 5°yaw starboard angle of attack case the turbulence has the same functional shape as the 0°angle of attack however the peak levels are approximately twice that seen in the 0°case. Phase averaged radial profiles for the two 5°cases at $x/D = 3.17$ were shown for the zero thrust condition and evidence of rotor effects were seen in the mean velocity for both configurations. The turbulence in the 5°pitch down case also exhibited rotor effects in the turbulence however no phase variation was noted in the 5°yaw starboard case. The PIV for an advance ratio of J=1.27 was examined and phase correlated structures were noted within the radial profile. These structures had an amplitude of about $\overline{u_x^2}/U_\infty^2 = 6\text{x}10^{-4}$ and repeated 6 times over the course of one rotor revolution, corresponding to a frequency of 533 Hz. The two-point correlation function at the rotor inlet for the various configurations were compared. The correlation function for the 0°angle of attack case was stretched in the streamwise direction and rotated clockwise 7°from the BOR x-axis, in comparison the 5°pitch down and yaw starboard angle of attack cases were rotated clockwise 18°and 16°respectively. The 5°pitch down case showed elongation through the rotor plane and significantly further upstream than both the 0°angle of attack and the 5°yaw starboard case. The evolution of the two point correlation along a streamline intersecting 75% of the rotor radius was shown for the 5°pitch down and yaw starboard angles of attack. In the pitch down case the correlation function increases its clockwise rotation angle and the length of its tail as the anchor points move downstream. In contrast the yaw starboard case shows less variation in rotation and deformation moving downstream.

Acknowledgments

The authors would like to thank the Office of Naval Research for sponsoring this work under grant N00014-20-1-2665, and specifically Drs. Yin Lu Youn, Ki-Han Kim and John Muench. Authors are particularly grateful to Dr Meng Wang and Dr Di Zhou at UND for the RANS CFD results that provided context to these data. Further acknowledgements go to Vidya Vishwanathan, Shishir Damani, Rachel Andrews, Aayush Salot, and Shivam Khullar amongst others for their assistance during the wind tunnel experiments. The authors would also like to thank Mr. Michael Marcolini for his ever present advice.

References

[1] Glegg, S. A. L., and Devenport, W. J., "Proper Orthogonal Decomposition of Turbulent Flows for Aeroacoustic and Hydroacoustic Applications," *Journal of Sound and Vibration*, Vol. 239, No. 4, 2001, pp. 767–784. https://doi.org/10.1006/jsvi.2000.3128.

[2] Glegg, S. A. L., Devenport, W., and Alexander, N., "Broadband rotor noise predictions using a time domain approach," *Journal of Sound and Vibration*, Vol. 335, 2015, pp. 115–124. https://doi.org/10.1016/j.jsv.2014.09.007.

[3] Glegg, S., Grant, J., Alexander, N., and Devenport, W., "Sound Radiation from a Rotor Operating in the Wake of a Cylinder," , 9-13 January 2017.

[4] Glegg, S., Pectol, J., Devenport, W., Alexander, N., and Molinaro, N. J., "Benchmarking of a Broadband Rotor Noise Prediction Method," , 8-12 January 2018.

[5] Majumdar, S., and Peake, N., "Noise Generation by the Interaction between Ingested Turbulence and a Rotating Fan," *Journal of Fluid Mechanics*, Vol. 359, 1998, pp. 181–216.

[6] Hanson, D., "Spectrum of Rotor Noise Caused by Atmospheric Turbulence," *Journal of the Acoustical Society of America*, Vol. 56, No. 1, 1974, pp. 110–136.

[7] Choi, K., and Simpson, R., "Some Mean Velocity, Turbulence, and Unsteadiness Characteristics of the VPISU Stability Wind Tunnel," Report, Virginia Tech, Department of Aerospace and Ocean Engineering, 1987.

[8] Devenport, W. J., Burdisso, R. A., Borgoltz, A., Ravetta, P. A., Barone, M. F., Brown, K. A., and Morton, M. A., "The Kevlar-walled anechoic wind tunnel," *Journal of Sound and Vibration*, Vol. 332, No. 17, 2013, pp. 3971–3991. https://doi.org/10.1016/j.jsv.2013.02.043.

[9] Hickling, C., Balantrapu, A. N., Millican, A. J., Alexander, N., Devenport, W., and Glegg, S., "Turbulence Ingestion into a Rotor at the Rear of an Axisymmetric Body," , May 20-23 2019.

[10] Balantrapu, A. N., Hickling, C., Alexander, N., and Devenport, W., "The structure of a highly-decelerated axisymmetric turbulent boundary layer," 2021.

[11] Hickling, C., "Inhomogeneous, Anisotropic Turbulence Ingestion Noise in Two Open Rotor Configurations," 2020.

[12] Renard, N., and Deck, S., "On the scale-dependent turbulent convection velocity in a spatially developing flat plate turbulent boundary layer at Reynolds number," *Journal of Fluid Mechanics*, Vol. 775, 2015, pp. 105–148. https://doi.org/10.1017/jfm.2015.290.

[13] Balantrapu, A. N., "The Space-time Structure of an Axisymmetric Turbulent Boundary Layer Ingested by a Rotor," 2021.

[14] Pope, S., *Turbulent Flows*, Cambridge University Press, 2000. URL https://books.google.com/books?id=HZsTw9SMx-0C.

[15] Banks, J. T., Butt, H., Balantrapu, N. A., Hickling, C., Alexander, W. N., Devenport, W. J., and Glegg, S. A., "A Comparison of Turbulence Ingestion of Axisymmetric and Non-Axisymmetric Wakes Into a Rotor," , 2022. https://doi.org/10.2514/6.2022-2528.